Bulletin of the Seismological Society of America, Vol. 104, No. 1, pp. 513–528, February 2014, doi: 10.1785/0120130136

The Attenuation of Fourier Amplitudes for Rock Sites in Eastern North America

by Gail M. Atkinson and David M. Boore

Abstract We develop an empirical model of the decay of Fourier amplitudes for earthquakes of **M** 3–6 recorded on rock sites in eastern North America and discuss its implications for source parameters. Attenuation at distances from 10 to 500 km may be adequately described using a bilinear model with a geometric spreading of $1/R^{1.3}$ to a transition distance of 50 km, with a geometric spreading of $1/R^{0.5}$ at greater distances. For low frequencies and distances less than 50 km, the effective geometric spreading given by the model is perturbed using a frequency- and hypocentral depth-dependent factor defined in such a way as to increase amplitudes at lower frequencies near the epicenter but leave the 1 km source amplitudes unchanged. The associated anelastic attenuation is determined for each event, with an average value being given by a regional quality factor of $Q = 525f^{0.45}$. This model provides a match, on average, between the known seismic moment of events and the inferred low-frequency spectral amplitudes at $R = 1$ km (obtained by correcting for the attenuation model). The inferred Brune stress parameters from the high-frequency source terms are about 600 bars (60 MPa), on average, for events of $M > 4.5$.

Introduction

A critical task for the development of ground-motion prediction equations (GMPEs), as used in seismic-hazard assessment applications, is the study of ground-motion attenuation, including the model for geometric and anelastic attenuation and its uncertainty. Of particular importance is the rate of attenuation at close distances (< 50 km) and the manner in which amplitudes at close distances transition to the levels observed at regional distances (> 100 km), where data are most plentiful.

This study is focused on defining a simple empirical attenuation model to describe the decay of Fourier spectral amplitudes in eastern North America (ENA) and its uncertainty. We pay particular attention to the issue of connecting data at close distances to regional data in a way that accommodates the physical constraint provided by seismic moment, while optimizing the fit to the ground-motion data amplitudes over a wide range of distances, at all frequencies. The model accommodates variability in the apparent rates of attenuation from one event to another that may arise due to the different crustal structures that are being sampled. The model focuses on the northeast area of ENA, as seismographic stations in this region are predominantly on rock sites, simplifying the problem by allowing attenuation to be examined without the added complications of site response on soil sites.

The study is motivated by the observations of Atkinson (2012), who showed that none of the existing attenuation models, including recent models by Boatwright and Seekins (2011) and previous models by Atkinson (2004) and Atkinson and Boore (1995), do an adequate job of matching the observed amplitude decay for the current (2012) ENA dataset as a whole (though the models may work well for individual events at some frequencies or over some distance ranges). We aim to improve on the modeling of attenuation by taking a fresh look at the overall problem of tying plentiful regional data to sparse near-distance data in a way that makes optimal use of what few constraints we have available. We begin with the regional distance range (> 150 km), where attenuation can be most confidently defined, using distant data to determine regional quality factor (Q); we find the best-fitting Q for each event at each frequency, thus ensuring a good match to the amplitude constraints on ground motion provided by the regional data. Based on previous studies and preliminary trials with alternative forms (including linear, bilinear, and trilinear forms, with hinge points at various distances), we choose a bilinear form of the attenuation model with the transition distance set at 50 km for the attenuation shape. We then find the slope (b) of the near-distance attenuation (assuming amplitudes decay from the source to 50 km as R^{-b}) that results in a match between the low-frequency spectral amplitude at $R = 1$ km and the value required by the known seismic moment of the event. We examine the residuals for this model to define apparent frequency-dependent trends that are revealed at closer distances; we use these trends

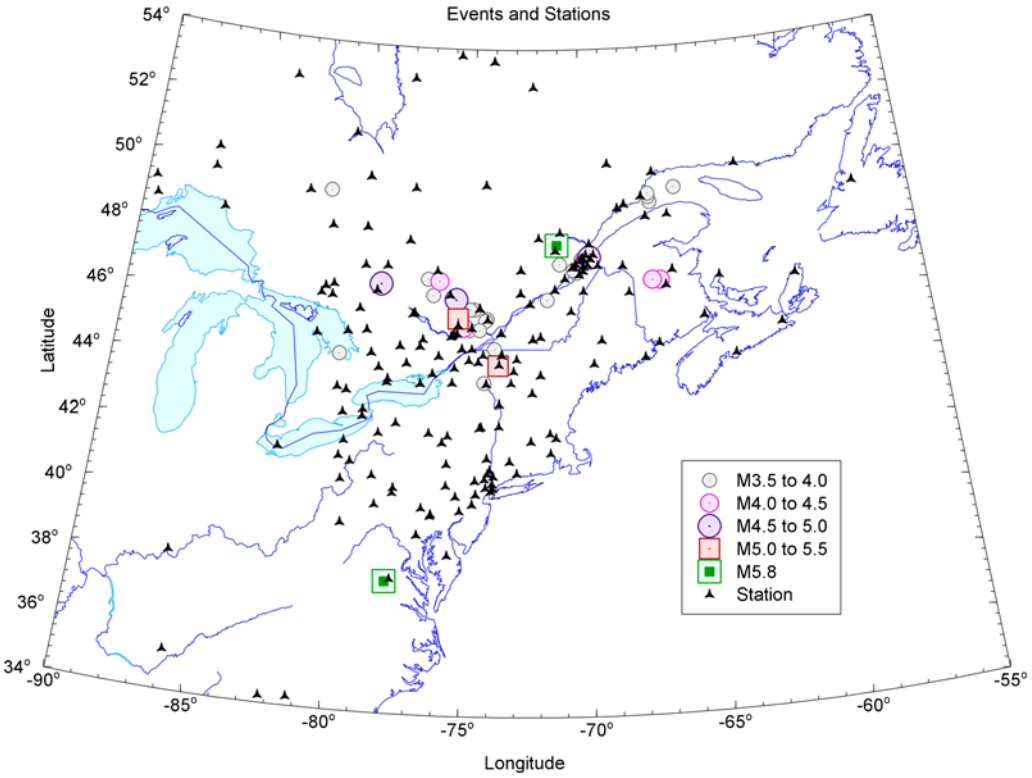

Figure 1. Locations of study events and recording stations. The color version of this figure is available only in the electronic edition.

to define a function that mimics frequency dependence in the effective geometric spreading at close distances, while leaving the 1 km source amplitudes unchanged. For each event, we correct the observations for the attenuation model to examine effective source spectra and their average shape for events of different magnitudes.

This study is part of a larger collaborative effort in the context of the Next Generation Attenuation-East Project (NGA-East Project), in which we are building new GMPEs by considering new information on source, path, and site constraints. This study outlines our work on the path component of this project and also touches on the implications of the attenuation model for the description of the earthquake source. It should be emphasized that this is strictly an empirical study. Numerical modeling studies that provide context for the attenuation trends we expect to observe are provided by Burger *et al.* (1987), Ou and Herrmann (1990), and Chapman (2012).

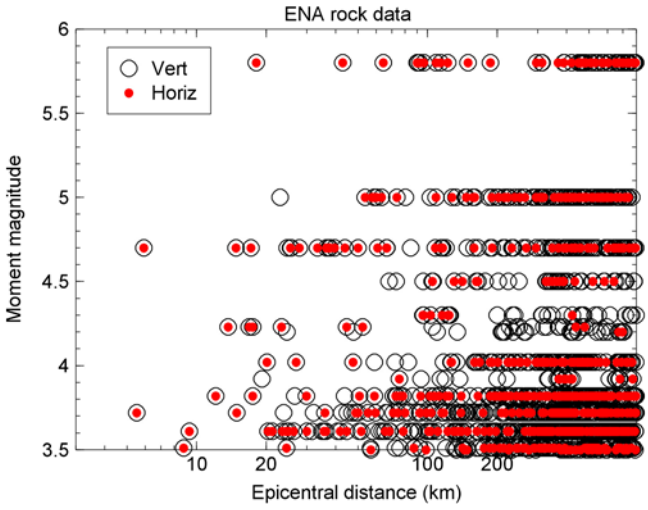

Figure 2. Distribution of available data in magnitude–distance space; data beyond 600 km were not used in this study. The color version of this figure is available only in the electronic edition.

Database for Study

The database for this study is the Fourier amplitude database for events in ENA as compiled and processed by Assatourians and Atkinson (2010; see Data and Resources), updated through 2011. Figure 1 shows a map of the events and stations, whereas Figure 2 shows the database distribution in magnitude and distance. For this study, we use records from events of moment magnitude (**M**) equal to or greater than 3.5, recorded on rock sites ($V_{S30} > 1000$ m/s, with most sites having $V_{S30} > 1800$ m/s), at distances up to 600 km. The horizontal component is the geometric mean of the two components. Fourier amplitudes were computed as described by Assatourians and Atkinson (2010) and smoothed in bins 0.1 $\log_{10}$ units in width. The moment magnitudes were taken from regional moment tensor inversions where available (such as those provided on B. Herrmann's website; see Data and Resources section); and **M** values were

estimated for the remainder of the events using a robust technique based on regional amplitude data, calibrated to events with known moment as described by Atkinson and Babaie Mahani (2013). The advantages of this technique are that the moment is based only on regional observations and is independent of the geometric spreading function or event-specific attenuation details.

Attenuation Behavior of ENA Fourier Amplitude Data

An empirical model for the Fourier acceleration spectrum as a function of magnitude and distance is the key component of stochastic models used to develop GMPEs. Typically, the acceleration spectrum is modeled by a spectrum with an ω^2 shape, in which ω is the angular frequency (Brune, 1970, 1971; Boore, 1983, 2003). The ω^2 model spectrum is derived for an instantaneous shear dislocation at a point. The acceleration spectrum of the shear wave, $Y(f)$, at an effective distance R from an earthquake is given by

$$Y(f) = CM_0G(R)\{[2\pi f]^2/[1 + (f/f_0)^2]\}A(f) \times \exp(-\pi f\kappa_0)\exp(-\pi fR/Q\beta), \quad (1)$$

in which M_0 is seismic moment and f_0 is corner frequency. The latter is given by $f_0 = 4.906 \times 10^6\beta(\Delta\sigma/M_0)^{1/3}$, in which $\Delta\sigma$ is the stress parameter in bars (where 10 bars = 1 MPa), M_0 is in dyn·cm, and β is the shear-wave velocity near the source, in km/s (assumed to be 3.7 in this article) (Boore, 1983). The constant C is generally taken as $C = \Re_{\theta\phi}FV/(4\pi\rho\beta^3)$, in which $\Re_{\theta\phi}$ is the radiation pattern (average value of 0.55 for shear waves), F free-surface amplification (2.0), V the partition onto two horizontal components (0.71), and ρ density (2.8) (Boore, 1983, 2003). The model in equation (1) is based on a point-source representation of the ground motion; however, as shown by several authors (e.g., Atkinson and Silva, 2000; Boore, 2009; Yenier and Atkinson, 2012; E. Yenier and G. M. Atkinson, unpublished manuscript, 2014), the model works well for predicting motions from sources of finite extent if the distance R is modified to account for geometric effects of a finite source. That is why we refer to R as an effective distance rather than a hypocentral distance. For small earthquakes R would be very nearly equal to the hypocentral distance, but for large earthquakes it would be larger than the hypocentral distance, resulting in a near-distance ground-motion saturation effect. In addition, when using the equation above to extrapolate observed motions back to the source, we set $R = 1$ km, even though this would not generally be realizable if R was truly the hypocentral distance. In other words, $R = 1$ km represents a virtual point-source location, not an actual point in physical space. Note that the specified values of physical constants are not particularly important, except that they act together to provide a scaling factor that connects observations to source and attenuation parameters. Thus, the same constants should be maintained when applying the model in a forward sense. $A(f)$ is the amplification from the source to the surface. For the very hard rock site conditions of interest to us in this article, this is a maximum of 1.4 for the horizontal component at high frequencies; it is assumed to be near unity for the vertical component (Atkinson and Boore, 2006). The kappa term, $\exp(-\pi f\kappa_0)$, is a high-cut filter to account for near-surface attenuation effects, which describe the commonly observed rapid spectral decay at high frequencies (Anderson and Hough, 1984).

$G(R)$ in equation (1) is the geometrical spreading function; it equals $1/R$ for a uniform whole space, but it can be a complex function of R. At close distances, the geometric spreading is controlled by the decay of direct-wave amplitudes in a layered crust, whereas at larger distances there are contributions from reflections and refractions from the Moho and a transition to surface-wave spreading (e.g., Burger *et al.*, 1987). For example, in Atkinson (2004), $G(R)$ is represented by a tripartite behavior that includes an increase in amplitude for distances between 70 and 140 km, due to postcritical angle reflections, followed by a transition to surface-wave spreading rates. It is generally agreed that geometric spreading may be modeled as $1/R^{0.5}$ in ENA at regional distances (> 100 km; i.e., the surface-wave spreading rate), but that attenuation due to geometric spreading decays more rapidly at close distances ($1/R^n$, with $n \geq 1$; e.g., Atkinson, 2012). The quality factor, $Q(f)$, is an inverse measure of effective anelastic attenuation, which introduces an additional decay in spectral amplitudes with distance; this attenuation is frequency dependent, and thus alters spectral shape.

The overall behavior of the data with respect to the standard model of equation (1) is illustrated in Figure 3, which shows plots of Fourier acceleration data for the 2005 **M** 4.7 Rivière du Loup event, in comparison with two commonly used attenuation curves. Both the vertical and geometric mean horizontal components are plotted; it is a well-documented observation that the attenuation trends of the components are very similar for rock sites in ENA and that the horizontal-to-vertical (H/V) ratio is stable and predictable on average, being near unity at low frequencies and rising to values near 1.4 at high frequencies (e.g., Siddiqqi and Atkinson, 2002). The reference models plotted on Figure 3 are both bilinear with a transition in slope of the geometric spreading at 60 km. Both models feature $1/R^{0.5}$ spreading beyond 60 km, with a constant $Q = 2000$ over all distances (Atkinson, 2012, showed that this is a representative Q value). For distances within 60 km one model has geometric spreading of $1/R$ (e.g., Boatwright and Seekins, 2011), whereas the other has geometrical spreading of $1/R^{1.3}$ (e.g., Atkinson, 2004). The crustal amplification is set equal to unity at all frequencies (appropriate for the vertical component, but an underestimate for the horizontal component at high frequencies). At low frequencies, the level of the curve is entirely determined by the constraint provided by the known seismic moment for the event (equation 1, which sets the amplitude at $R = 1$ km). This places significant

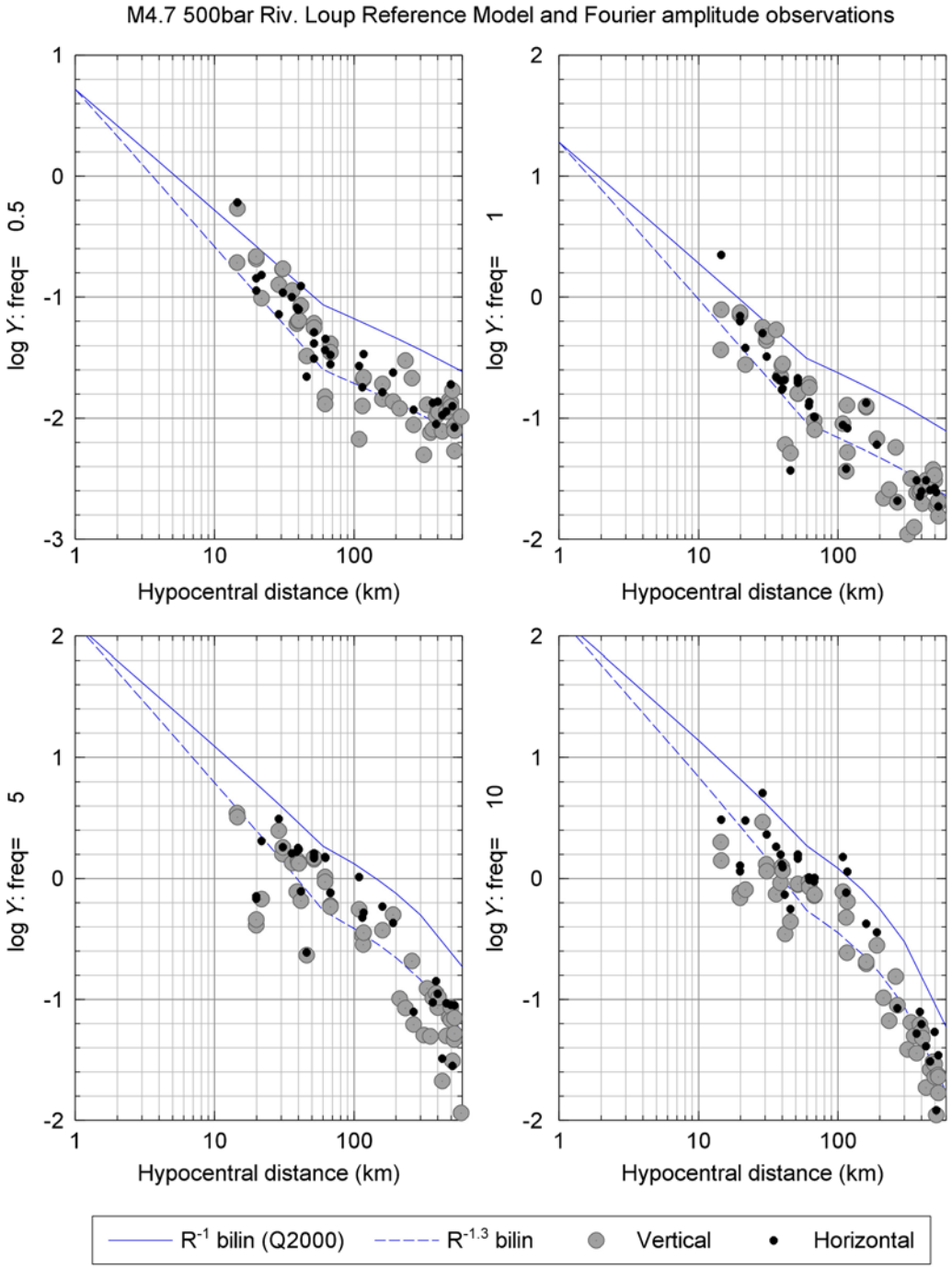

Figure 3. Fourier amplitude data for 2005 **M** 4.7 Rivière du Loup event for frequencies of 0.5, 1, 5, and 10 Hz. Two reference attenuation models are shown, calculated for $\mathbf{M} = 4.7$, for 500 bar stress value, using equation (1). Both attenuation models have $1/R^{0.5}$ geometric spreading at $R > 60$ km, with constant $Q = 2000$ at all distances. One model has $1/R^{1.0}$ attenuation at close distances, whereas the other has $1/R^{1.3}$ attenuation at close distances. The color version of this figure is available only in the electronic edition.

constraints on the attenuation models that will match the data. For example, it is apparent in Figure 3 that the bilinear model with $1/R$ to 60 km overpredicts low-frequency amplitudes; this overprediction comes entirely from the inability of this form to match the moment constraint.

The $1/R$ model also overpredicts high-frequency amplitudes on Figure 3. At high frequencies, the level of the curve is affected by both moment and stress drop. The stress parameter is arbitrarily set at 500 bars for the results shown in Figure 3. The high-frequency decay parameter, set at $\kappa_0 = 0.005$ s, likewise affects only the high frequencies. (This can be easily shown from equation 1.)

It is important to note that the 2005 Rivière du Loup earthquake is the only event in the dataset that has sufficient

ground-motion data to adequately see the effective attenuation curve over the entire range of distances from near source (< 20 km) to regional distances within a single event. For other events, data must be combined over multiple events in order to describe the attenuation. The manner in which such data may be combined to best bring out the underlying attenuation characteristics is a challenging problem, which we address in this study.

Although data are sparse at close distances, they are plentiful at regional distances (> 100 km). Moreover, the data tend to be well behaved in their attenuation trends at regional distances, as shown by many studies (e.g., Ou and Herrmann, 1990; Atkinson, 2004, 2012; Babaie Mahani and Atkinson, 2012). However, inspection of plots such as those shown in Figure 3 on an event-by-event basis reveal differences from one event to another in the observed anelastic attenuation parameter (curvature of the line away from the $R^{-0.5}$ line in log–log space). These differences likely reflect the interplay between a number of factors, including regional variability of anelastic attenuation, source directivity effects, focal depth effects, and the geographic distribution of stations for the particular event, with respect to the source. This variability is important, as it will map into uncertainty in near-source amplitudes, if we wish to use regional amplitude data to infer near-source amplitudes. Therefore, we consider the anelastic attenuation coefficient separately for each event, so that we can more accurately correct the regional observations to near-source distances.

Effective Anelastic Attenuation and Its Variability

To explore the variability in inferred anelastic attenuation that is seen from one event to another and to facilitate the inspection of geometric spreading after removal of such effects, we used just the regional data (within the 150–500 km distance range) to determine the anelastic attenuation parameter for each event, which we refer to as the effective anelastic attenuation. The vertical component data are used for this exercise, as they are most plentiful; note that the H/V ratio shows no distance trends in this distance range (Siddiqqi and Atkinson, 2002), so the results are not sensitive to which component is selected. The results are also relatively insensitive to the distance range selected. Similar results were obtained for the 200–600 km distance range, though there is a tendency toward finding slightly gentler attenuation rates as the distance range is moved out toward larger distances; this trend was also noted by Boatwright and Seekins (2011) and is likely a consequence of the increasing contributions of noise at larger distances.

The data for each event having at least five observations in the 150–500 km distance range are fit to a variation of equation (1) formulated for application to the regional distance range:

$$\log Y(f) + 0.5 \log R = c_i(f) + g_i(f)R, \qquad (2)$$

in which $\log Y(f)$ is the log(base10) of the observed Fourier acceleration amplitude (cm/s; vertical component) at frequency f, R is the effective distance from the source (km), and $g_i(f)$ is the effective anelastic attenuation constant for event i (for a given frequency). The level of the curve is set by $c_i(f)$, which is an event-amplitude term. The term $+0.5 \log R$ on the left side of equation (2) adjusts all amplitudes for an assumed geometric spreading of $1/R^{0.5}$, which corresponds to surface-wave spreading in a half-space (e.g., see Atkinson, 2012, for discussion). Note that the anelastic attenuation coefficient is inversely proportional to the quality factor, Q:

$$g_i(f) = -(\pi f)/(2.3 Q_i \beta), \qquad (3)$$

in which f is frequency (Hz) and β is the crustal shear-wave velocity (assumed = 3.7 km/s; see Atkinson and Boore, 2006; this velocity can be different than the shear-wave velocity near the source, in equation 1, although we use the same value of 3.7 km/s for both in this article). We imposed the constraint that g_i must be negative. In other words, the attenuation line must curve down, not up, as distance increases; if a positive value of g_i was obtained for an event, it was reset to $g_i = 0.0$. Figure 4 shows the obtained values of g_i for selected frequencies. The scatter of values is significant (partly due to the combination of stochastic variability and limited sampling), but the average values are consistent with those found in previous studies.

Figure 5 plots the mean and standard deviation of the Q values computed from the g_i values. Only the g_i values for events of $\mathbf{M} \geq 4$ were used to determine the mean Q; this restriction was imposed to minimize the noise bias in the attenuation rates that is suggested by inspection of Figure 4 (particularly at lower frequencies). Two typical regional Q models, as determined by Atkinson (2004) and Boatwright and Seekins (2011), are also shown on Figure 5. These Q models are typical of those for stable continental interiors, which are characterized by higher Q values than are more active tectonic regions (e.g., Benz *et al.*, 1997). The study by Atkinson (2004) used data out to larger distances than that by Boatwright and Seekins (2011) (800 versus 600 km), as well as using a larger more geographically variable database. As noted by Boatwright and Seekins (2011), the curve obtained for Q may shift up or down somewhat depending on the distance range selected. For example, a sensitivity test of the results on Figure 5 showed that using the 200–600 km distance range (instead of 150–500 km) had the effect of shifting Q values up by ~200—probably due to the greater noise included at larger distances. A least-squares best-fit line to the mean Q values plotted on Figure 5 is

$$Q = 525 f^{0.45}. \qquad (4)$$

Geometric Spreading for $R < 150$ km

We can correct all observations to remove attenuation using the $g_i(f)$ terms for that event, plus any specified overall

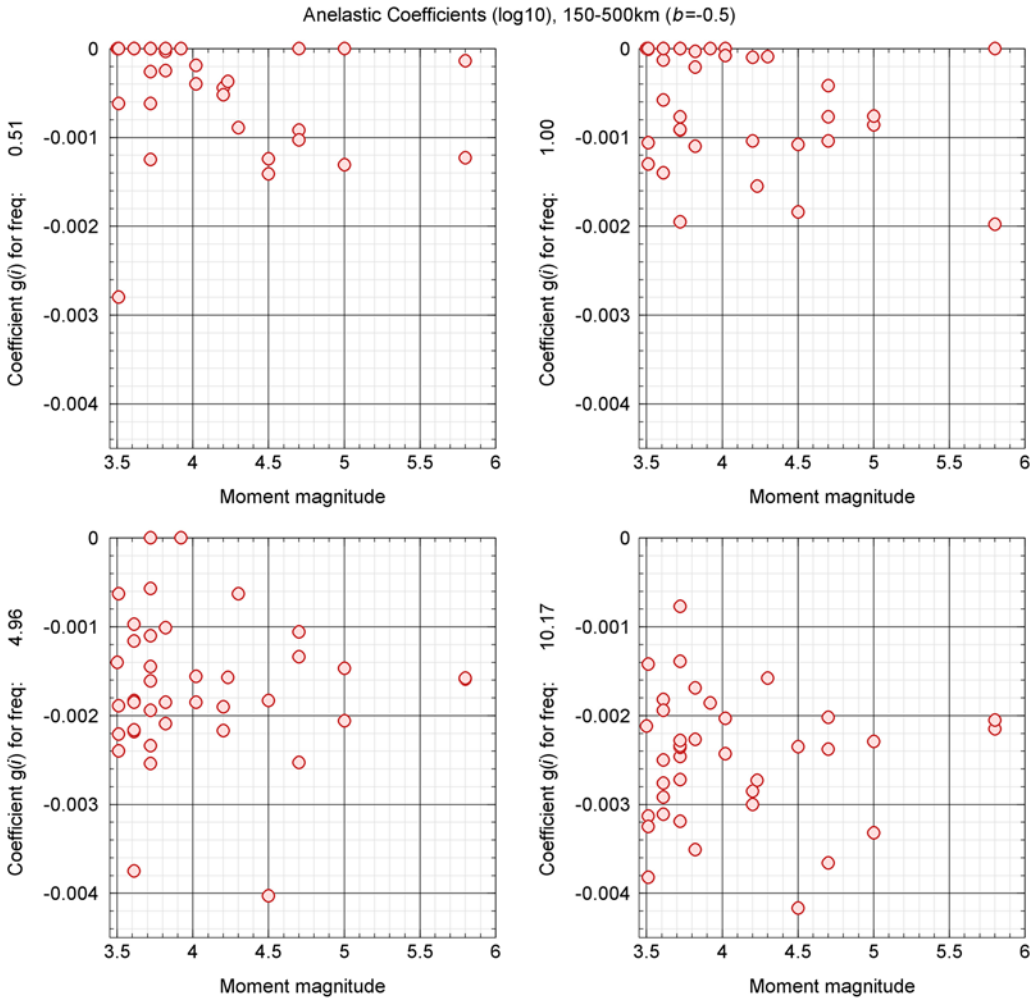

Figure 4. Value of effective anelastic coefficient (g_i), as determined for events with five or more observations in the 150–500 km distance range, at frequencies 0.5, 1, 5, and 10 Hz. Each symbol represents the value determined for an individual earthquake. Note that the Mineral Springs, Virginia, event has been included here, even though we do not know the site conditions for most of its stations; it is the higher (less negative) of two g_i values plotted at **M** 5.8 (with the lower being the 1988 Saguenay, Quebec, event). The values of g_i are set to 0.0 if the regression analysis yielded values greater than 0.0. The color version of this figure is available only in the electronic edition.

geometric spreading model, then examine the attenuation residuals with respect to that model to discern any trends or misfits (where residual $= \log(Y_{\text{observed}}) - \log(Y_{\text{predicted}})$; note that we use base-10 logs throughout). The reason we use the individual $g_i(f)$ terms to correct for anelastic attenuation, rather than the more conventional approach of applying an average regional anelastic attenuation model, is to force a zero trend in the residuals at regional distances (where anelastic attenuation is the dominant effect), for all events. This allows us to more effectively isolate the remaining attenuation trends at closer distances. A good initial indication of the attenuation shape that will be required can be obtained by looking at the residuals that are obtained if we apply the regional-distance $1/R^{0.5}$ geometric spreading function, with the event-based $g_i(f)$ values, over all distances. What we would expect to see in such a plot is a zero-trend in residuals on average over the 150–500 km distance range (over which the attenuation model was defined). We would expect to see significant positive residuals as we move from 150 km in toward the source, because we expect the geometric spreading coefficient to be significantly larger than 0.5 at close distances. Such a plot is provided in Figure 6 and does indeed show the expected trends. However, a feature of the plot that we did not expect is the clear evidence for apparent frequency dependence of the geometric spreading rate. At $R < 50$ km, the residuals have larger amplitudes at low frequencies than they do at high frequencies. Because the anelastic part of the attenuation has been removed by correcting all observations using the$g_i(f)$ terms, the trends are controlled by geometric spreading and suggest that it is frequency dependent at close distances.

It is also noteworthy that the inferred shape of the attenuation curve is not consistent across frequencies. At low frequencies, we would infer a trilinear shape based on the negative residuals from ~70 to 150 km, transitioning to positive residuals at close distances; at higher frequencies the

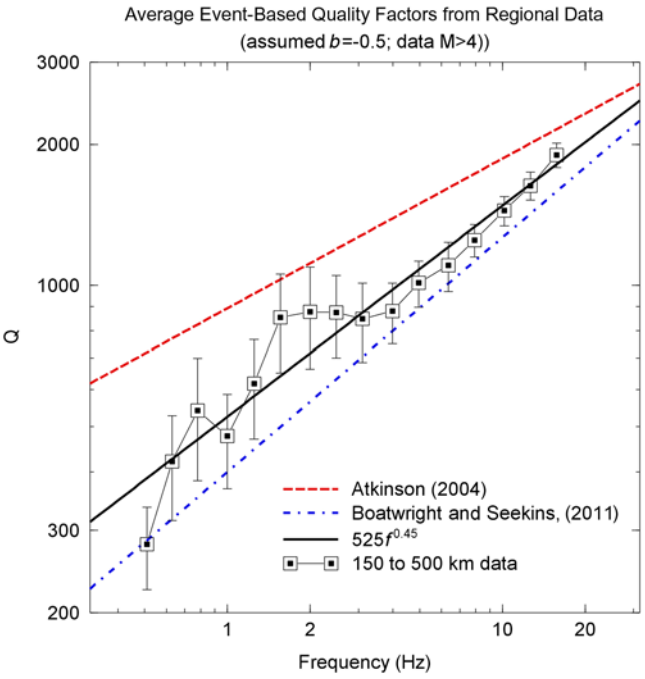

Figure 5. Means and standard deviations of event-based Q values, determined from data 150–500 km for $\mathbf{M} \geq 3.5$. The Q models of Atkinson (2004) and Boatwright and Seekins (2011) are shown for comparison. The best fit to mean Q values is given by $Q = 525f^{0.45}$. The color version of this figure is available only in the electronic edition.

evidence for a trilinear attenuation shape diminishes, and tends to suggest a bilinear shape is required. Based on this evidence, we judge that there is little advantage to use a trilinear form—it would improve the residuals slightly at low frequencies, but at the cost of additional complexity and the need to determine more parameters (two hinges, two geometric spreading slopes). We therefore conclude, as did Babaie Mahani and Atkinson (2012), that the bilinear form strikes the optimal balance between an overly simplistic model and one that accounts for all of the complexity in the attenuation behavior. In other words, while there is evidence that the attenuation form is trilinear, at least at lower frequencies, the evidence is not sufficiently compelling to warrant the added complexity of the additional parameters that must be specified for the trilinear form.

We considered alternative values of the transition distance (from 40 to 150 km), and alternative values of the near-distance geometric spreading parameter (from 1.0 to 1.5), to find combinations that remove the residual trends seen on Figure 6 to the extent possible, while satisfying the moment constraint on average for lower frequencies. The residual trends strongly favor transition distances less than 70 km, which is not surprising given previous studies (e.g., Atkinson, 2004, finds the first hinge of a trilinear model is near 70 km, whereas Boatwright and Seekins, 2011, find the best hinge point for a bilinear model is near 50 km). To provide the best shape for the residual trends, we make the initial assumption that the transition distance will be near 50 km. It then remains to find the near-distance slope that will satisfy the moment constraint, fine-tuning the transition distance if required. For each potential value of the near-distance slope (1.0, 1.2, 1.3, …), we find the misfit to the moment end of the Fourier spectrum (frequencies from 0.5 to 1.0 Hz). This misfit is minimized on average, for events of $\mathrm{M} \geq 3.5$, for a near-distance slope of 1.3. An important observation is that a geometric spreading function decaying as R^{-1} from the source cannot match the moment constraint, because the amplitudes at the lowest frequencies (0.5–1 Hz) are overpredicted at regional distances with this model, even if the transition distance is moved all the way out to 150 km. On this basis, we choose a bilinear function that decays as $R^{-1.3}$ to 50 km, then as $R^{-0.5}$ at greater distances. A slightly smaller geometric-spreading slope (e.g., 1.1–1.2) could satisfy the moment constraint if the transition distance were moved out to a larger distance, but does a poorer job of matching the shape of the residual trends.

Overall, we conclude that a near-distance geometric spreading of $1/R^{1.3}$ with a transition distance of ∼50 km provides the best balance between minimizing the overall bias in low-frequency amplitudes (0.5–1 Hz), while also minimizing residual trends versus distance to the extent possible, over all frequencies and distances. Using this bilinear geometrical spreading function, we adjust each observation for attenuation to compute attenuation-adjusted amplitudes:

$$\log Y'_{ij}(f) = \begin{cases} \log Y_{ij}(f) + 1.3 \log R_{ij} - g_i(f) R_{ij} & R \leq 50 \text{ km} \\ \log Y_{ij}(f) + 1.3 \log 50 + 0.5 \log(R_{ij}/50) - g_i(f) R_{ij} & R > 50 \text{ km} \end{cases}, \quad (5)$$

in which i is an event index and j is a station index (and $g_i(f)$ is negative in sign). The mean value of $\log Y'_{ij}(f)$ for each event, taken here using only the regional observations ($R_{ij} > 150$ km), is an estimate of the event term. If we subtract the event term from $\log Y'_{ij}(f)$, we obtain the residuals for our event-based effective anelastic attenuation model with the fixed bilinear geometric spreading model. The residuals will have no trends in the distance range in which the data were fitted to derive the effective anelastic model (150–500 km). However, if we plot the residuals from the regional attenuation model at closer distances, $R < 150$ km, we can see any deviations of the geometric spreading model

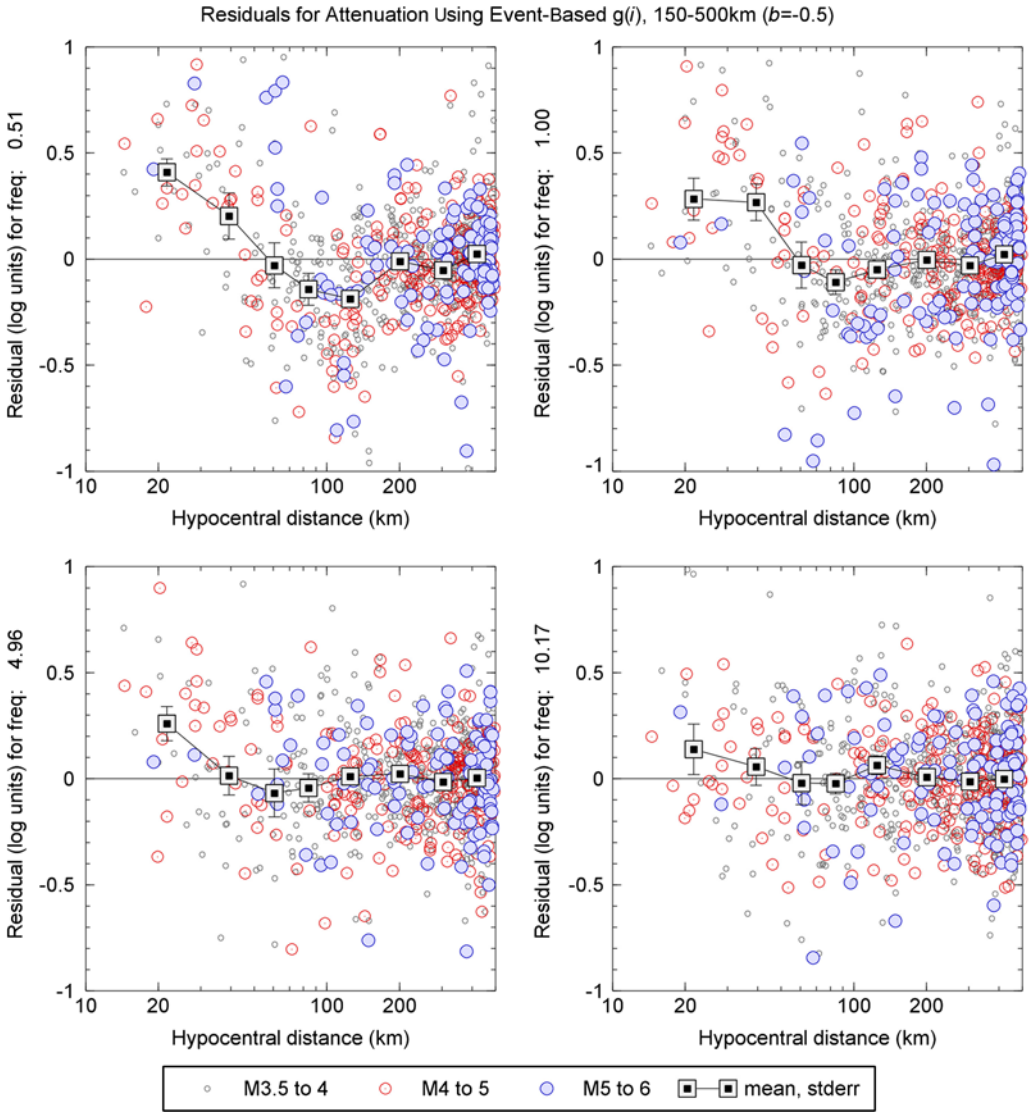

Figure 6. Residuals obtained assuming $1/R^{0.5}$ geometric spreading function with the event-based $g_i(f)$ values over all distances. Symbols with error bars show the mean and standard error of residuals in distance bins with end points at 30, 50, 70, 100, 150, 250, 350, and 500 km. The color version of this figure is available only in the electronic edition.

from the assumed form. Because the model is effectively pinned at regional distances, positive residuals at close distances indicate that the near-distance attenuation rate is not steep enough—we have not provided a sufficient correction to reach the observed amplitudes, and this results in underprediction. Conversely, negative residuals at close distances imply that the data are suggesting a less rapid attenuation than that given by $1/R^{1.3}$.

It is important to emphasize that we use only the regional observations ($R > 150$ km) to estimate the event terms. This has several advantages. First, the regional observations are the most stable and well behaved, and thus the overall level at regional distances is likely the best indicator of overall source strength (see Shin and Herrmann, 1986; Ou and Herrmann, 1990; Atkinson, 2012). Furthermore, consistent application of this practice ensures that there is no bias in source terms obtained based on availability or lack thereof of near data. Finally, it means that the shape of the source terms and their relative amplitudes between events are fixed, with the level of the source amplitudes scaling by a constant that depends on the assumed geometric spreading model within 150 km. This facilitates identification of the geometric spreading rate that will scale the source terms to the correct level as given by the moment constraint.

Figure 7 plots the residuals calculated as described above, along with the mean and its standard error in distance bins. As expected, the residuals are zero on average for distances beyond 150 km. However, we have not been entirely successful in removing the frequency dependence in residual trends (which was also seen in Fig. 6). The residuals are near zero (or slightly negative) at 5–10 Hz, but there is still a slight trend in the low-frequency residuals (reflecting the apparent

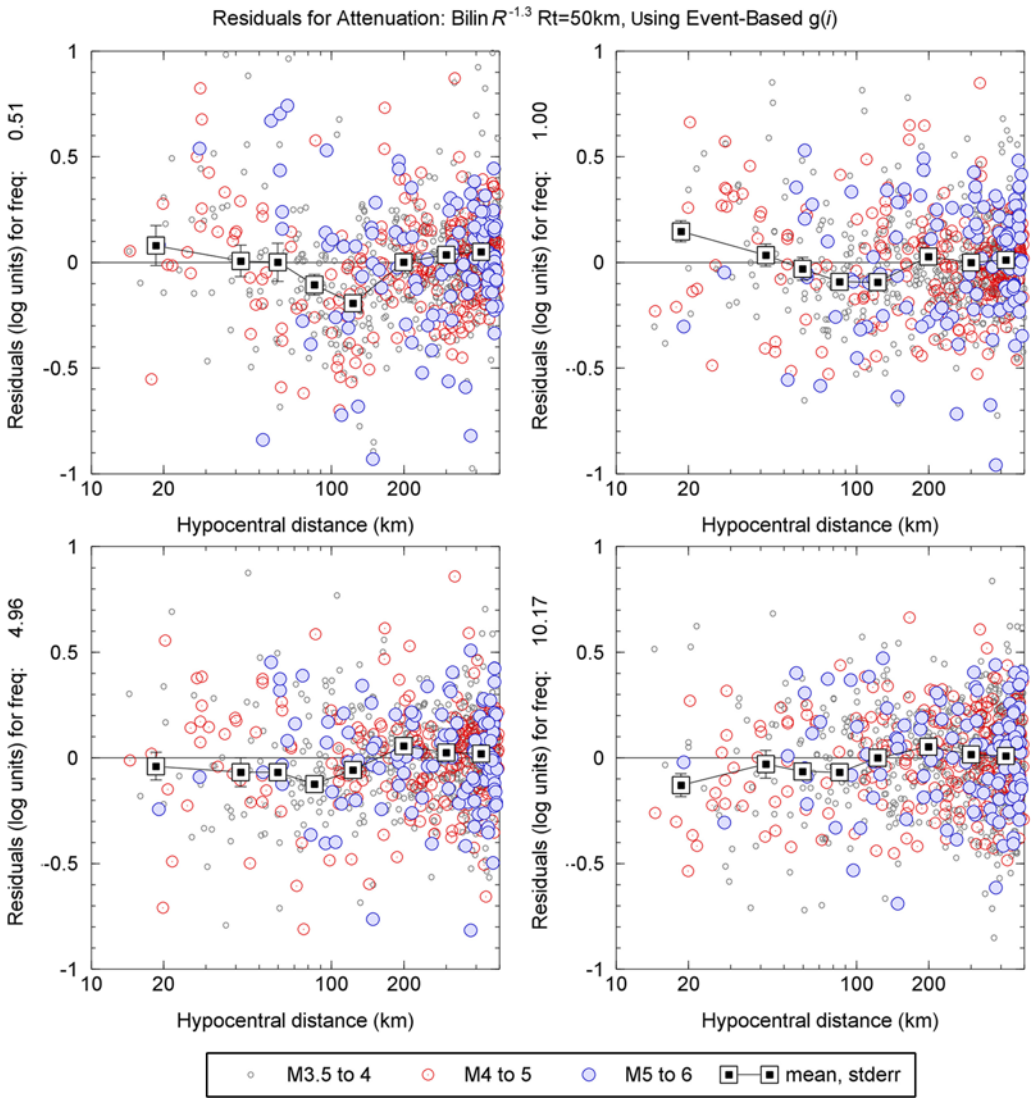

Figure 7. Residuals obtained when amplitudes are adjusted for a bilinear geometric spreading model ($1/R^{1.3}$ to 50 km, $1/R^{0.5}$ beyond), with event-based effective anelastic term. Symbols with error bars show the mean and standard error of residuals in distance bins with end points at 30, 50, 70, 100, 150, 250, 350, and 500 km. The color version of this figure is available only in the electronic edition.

trilinear shape feature that we chose to ignore) and a tendency to positive residuals at close distances. This would imply a more rapid effective geometric spreading at low frequencies. We use the term "effective geometric spreading" to stress that this is purely an empirical description of how the amplitudes appear to decay and not necessarily a reflection of the true underlying geometric spreading. For example, the positive residuals at close distances at lower frequencies might be reflecting average radiation pattern and directivity effects that do not average out over the focal sphere. Further study of the reasons for apparently high amplitudes at close distances and their frequency dependence is underway and will be the subject of a future paper.

The apparent nature of the geometric spreading at $R < 150$ km is interesting. At high frequencies, the residuals are slightly negative, while they are positive at low frequencies. At lower frequencies, there is some evidence for a trilinear form in the geometric spreading. This is particularly pronounced for the lowest frequencies (0.5–1 Hz), as positive residuals at 20 km become negative residuals near 100 km, before returning to 0 residuals at $R > 150$ km. This supports the trilinear shape noted previously by Atkinson (2004) and Atkinson and Mereu (1992). However, the evidence for a trilinear shape washes out as frequency increases.

The frequency dependence of the effective geometric spreading is further illustrated in Figure 8, which plots the average residuals in distance bins versus frequency. Note that for frequencies of 5 Hz and greater, the attenuation model produces average residuals with a slightly negative bias at close distances. At low frequencies, there is a positive bias at close distances and a negative bias near 100 km (while estimates are nearly unbiased at 60 km and beyond 150 km). We reiterate that the residuals do not necessarily imply true frequency dependence in the geometric spreading, only in its

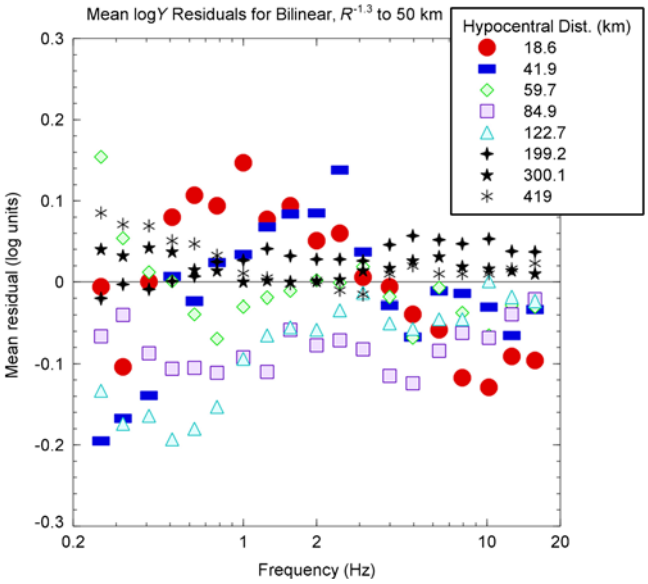

Figure 8. Mean bias (log units) for binned residuals, with respect to geometric spreading model of $1/R^{1.3}$ to 50 km, $1/R^{0.5}$ beyond, with event-based anelastic attenuation terms. The color version of this figure is available only in the electronic edition.

effective value as determined here. For example, we have assumed that the Q model calculated from regional observations also holds at closer distances. If Q was dependent on distance, this could map into an apparent frequency dependence of geometric spreading.

There are several possible ways that frequency dependence in the effective geometric spreading rate near the source might be parameterized, including different geometric spreading slopes as a function of frequency and/or the use of different distances at which to transition to $1/R^{0.5}$ spreading. Either bilinear or trilinear forms could be considered. However, at low frequencies not all forms will obey the moment constraint, as discussed earlier. These were the issues that were balanced in concluding that a reasonable choice is to use the bilinear model ($1/R^{1.3}$ to 50 km, $1/R^{0.5}$ beyond). However, in order to accommodate the remaining residuals, the predicted near-distance ($R < 50$ km) amplitudes should be multiplied by a frequency-dependent empirical adjustment function. The adjustment function is used to reproduce the observed higher amplitudes at low frequencies at close distances, without actually changing the geometric spreading term or the implied source amplitudes. From inspection of Figure 8, we define a low-frequency adjustment factor C_{LF}, which modifies the amplitudes for $f \leq 1$ Hz. In log units we have

$$C_{\mathrm{LF}} = \begin{cases} 0.2\cos\left(90\frac{R-h}{1-h}\right) & R \leq h \\ 0.2\cos\left(90\frac{\min(R,50)-h}{50-h}\right) & R > h \end{cases} \quad (6)$$

for cosine in degrees (replacing 90 with $\pi/2$ if the cosine is being computed in radians), in which h is focal depth and R is the effective distance from the source (see the discussion below equation 1). The reason focal depth is introduced is to provide a function in which the near-distance amplitudes are increased at zero surface distance (i.e., at the epicenter), but not at the source itself (i.e., $R = 1$ km); an arbitrary focal depth that is typical for the region can be assumed. C_{LF} attains a maximum value of 0.2 log units (factor of ~1.6 in amplitude) at 0.0 km epicentral distance and decays to 0.0 log units for $R \geq 50$ km. Equation (6), for the hypothetical observations at $R < h$, is written to emphasize that the function is forced back to 0.0 log units (factor of unity) at $R = 1$ km, so that the source amplitudes are unaffected. In other words, this function affects observed low-frequency observations at near-epicentral distances but is not considered a source effect.

We choose to taper the low-frequency factor as frequency (f) increases beyond 1 Hz, such that it is 0.0 log units at $f \geq 5$ Hz. It is acknowledged that this is a somewhat conservative choice, implying there will be a negative bias in high-frequency amplitudes at close distances (i.e., we are modeling the positive residual trends on Fig. 7, but not the negative trends). Thus we define a taper function that has a value of 1.0 for $f \leq 1$ Hz, declining linearly (in log–log space) to a value of 0.0 for $f \geq 5$ Hz:

$$T_C = \max[(1 - 1.429\log[\max(f, 1)]), 0]. \quad (7)$$

To predict Fourier amplitudes using the model, we multiply equation (1) by the new factor, $F(f, R)$, such that

$$\log F(f, R) = T_C C_{\mathrm{LF}}. \quad (8)$$

It may be noted that application of this factor is equivalent to having a geometric spreading at <50 km that depends on frequency, according to the following equation:

$$G'(R, h, f) = 10^{T_C C_{\mathrm{LF}}} G(R). \quad (9)$$

Using this equation, we note that extrapolation to the source (1 km) of motions at distances beyond 50 km produces the same source amplitude as those obtained using the function $G(R)$ ($G(R) = 1/R^{1.3}$ in our case), and thus the moment constraint at close distances is maintained. The (frequency-dependent) differences in the two geometric spreading functions appear only for distances between 1 and 50 km, as shown in Figure 9.

Application of the adjustment function of equation (8) removes the low-frequency bias in the residuals at distances less than 50 km. Note that we did not attempt to model the tendency to overprediction of amplitudes near 100 km. We accept the overprediction of amplitudes near 100 km as a reasonable compromise to avoid making the functional form more complex (i.e., using a trilinear model in addition to the apparent frequency dependence in the near-distance amplitudes).

Figure 10 compares the adopted bilinear attenuation model with the Rivière du Loup amplitude data and shows

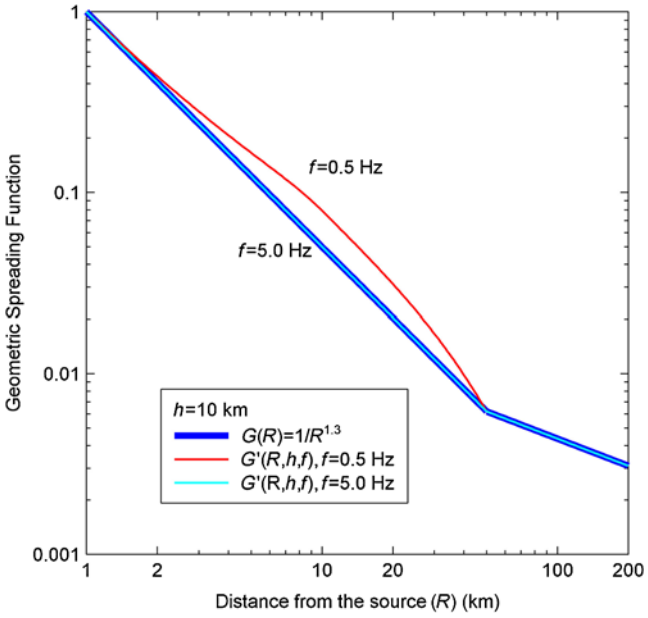

Figure 9. Standard geometric spreading, $G(R)$, and the effect of introducing frequency-dependent geometric spreading function, $G'(R, h, f)$, for a hypocentral depth of 10 km and frequencies of 0.5 and 5.0 Hz. The color version of this figure is available only in the electronic edition.

the effect of the frequency-dependent effective geometric spreading adjustment factor. The line is from equation (1) with the bilinear model used in equation (5) and the event-based attenuation; the squares are from equation (1), but using the effective geometrical spreading function of equation (9). The positive residuals with respect to the line are clearly seen at low frequencies at <50 km. The use of the frequency-dependent geometrical spreading correction factor largely removes the positive bias in the residuals for distances less than 50 km. Note that no crustal amplifications are applied, but these would be negligible for the vertical component and also negligible for the horizontal component at low frequencies. The prediction model is reasonably consistent with the spectral amplitudes at all frequencies and distances.

In Figure 10, the amplitude levels and shape of the prediction lines are controlled by: (1) the known seismic moment, which fixes the near-source amplitude levels at low frequencies; (2) the stress parameter, which scales the high-frequency amplitudes near the source; (3) the effective geometric spreading model; and (4) the $g_i(f)$ values for the Rivière du Loup event (sets the shape of the curves at regional distance). For forward modeling of a future event of a specified moment, we would not know the exact values of stress parameter or of $g_i(f)$. In this case, if we wished to forecast average amplitudes, we would apply mean values of stress and anelastic attenuation. Alternatively, if we wished to sample aleatory variability, we could apply the distribution of stress and $g_i(f)$ values in simulations. We note that the results in this paper provide data on those distributions.

Source Parameters Inferred from Ground-Motion Observations

The developed bilinear model describes the effective attenuation of Fourier amplitudes from source-to-site distances of ~15 km to regional distances (500 km). We can also use the model to infer the effective source amplitudes (at $R = 1$ km) for each event, by correcting for the attenuation effects and taking the average level at the source. As described in the previous section, the event terms determined from the vertical-component regional data (150–500 km) are used to define the source amplitudes, due to their robustness and stability. From equation (5), we can write the effective source amplitude for event i as

$$\log Y_{SRC_i}(f) = \frac{1}{N(i)} \sum_{j=1}^{N(i)} [\log Y_j(f) + 1.3 \log 50 + 0.5 \log(R_j/50) - g_i(f) R_j], \quad (10)$$

in which the sum is taken over $N(i)$ observations, collected at stations $j = 1, N(i)$, at distances R_j from 150 to 500 km for event i. This equation does not depend on the geometrical spreading modification in equation (8), because the adjustment only applies for recordings within 50 km. We use the vertical component of motion as a proxy for the horizontal, because any amplification effects due to passage through the near-surface velocity gradient are minimized (e.g., Lermo and Chavez-Garcia, 1993); furthermore, vertical-component data are more plentiful. The selection of the vertical component is not critical here, as the horizontal and vertical component amplitudes would imply similar source amplitudes, if we assume the average H/V ratio is simply the crustal amplification effect (e.g., Atkinson and Boore, 2006); as noted previously, the horizontal and vertical components attenuate in the same manner.

Figure 11 plots the effective source spectrum (at 1 km) inferred from the **M** 4.7 Rivière du Loup event, based on correcting for the attenuation model for the vertical-component regional observations. Error bars (barely visible at most frequencies) show the standard error of the source amplitudes, computed from the standard deviation of the mean amplitude, divided by the square root of the number of observations (minus one). It is the number of observations that results in small standard errors, as the standard deviation is significantly larger (~0.2 log units). The actual uncertainty in the effective source amplitudes would be larger than indicated by the standard error of the estimates, as it should also include uncertainty in the applicability of the model, which is difficult to assess. The effective source spectrum is in reasonable agreement with a Brune source model for **M** 4.7, with the inferred stress parameter being a little less than 500 bars, though we note a deficit in spectral amplitudes near 2 Hz, suggestive of source complexity.

Other examples of effective source spectra are shown in Figures 12 and 13, for events of **M** 5.0 (Au Sable Forks and

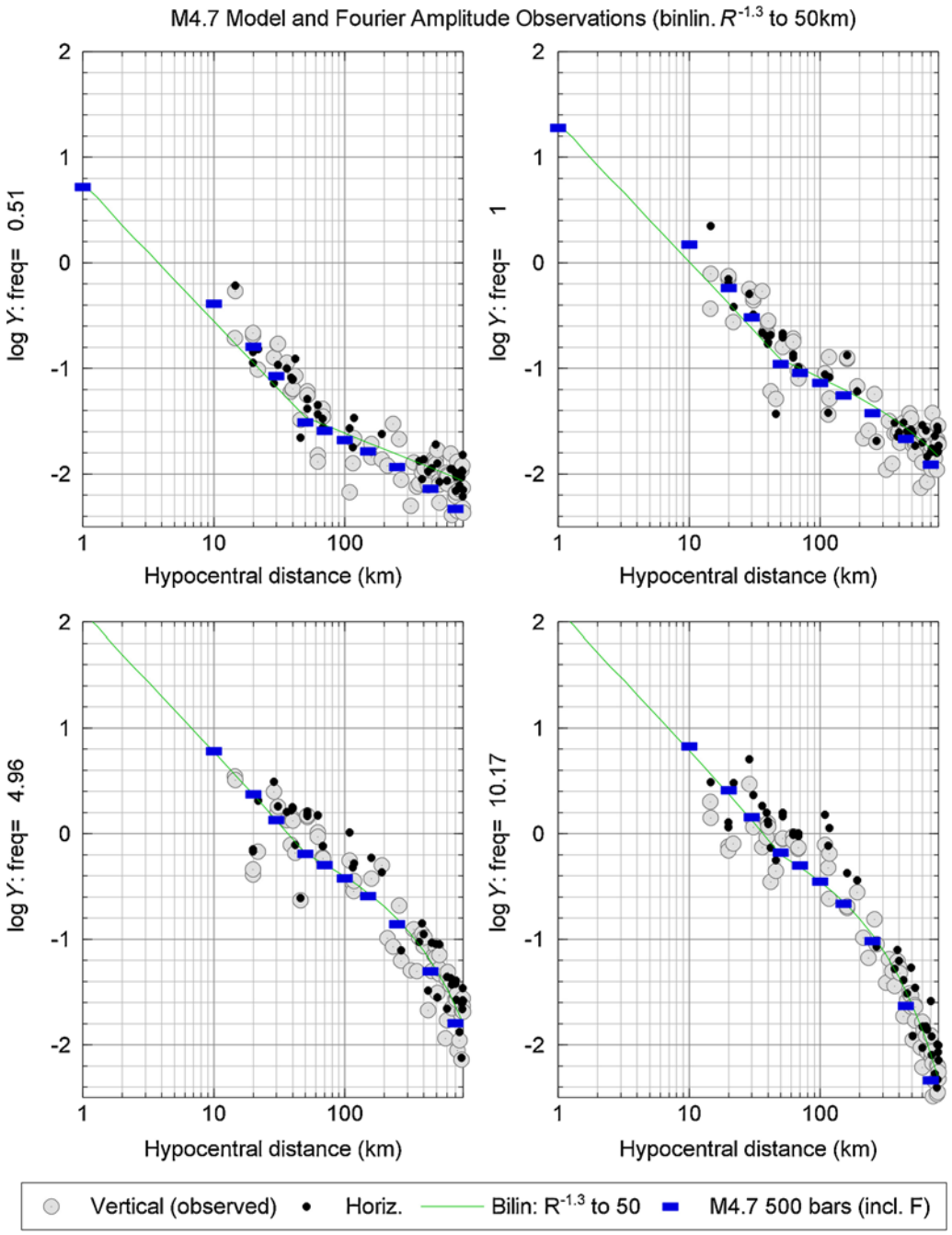

Figure 10. Fourier amplitude data from **M** 4.7 Rivière du Loup (circles) compared with Brune model predictions for **M** 4.7, 500 bars, including adjustment factor F (squares; no crustal amplifications applied). The line shows the standard bilinear model ($1/R^{1.3}$ to 50 km, $1/R^{0.5}$ beyond) with an event-based anelastic attenuation term, attenuated from the source using the regionally determined event terms. The color version of this figure is available only in the electronic edition.

Val-des-Bois) and **M** 5.8 (Saguenay and Mineral Springs). Poorly recorded events, such as the Saguenay and Au Sable Forks events, have very jagged source spectra with much variability, reflecting uncertainty in the actual levels of the effective source spectra.

For all four of the events in Figures 12 and 13, the overall level of the amplitude spectrum at low frequencies is slightly higher than the theoretical level for the known moment, implying that a shift in the spectrum to match the Brune level at low frequencies is required. This is equivalent to a required change in the constant C of equation (1) that equates observed amplitudes with Brune-model parameters. In Figure 14, we plot the approximate amount (in log units) by which the constant C must be adjusted to make the Brune model spectrum match the effective source spectrum at low frequencies. For small events (**M** <4.5), we calculated this factor based on the effective adjustment required at frequencies near 1 Hz, because the lower-frequency amplitudes are

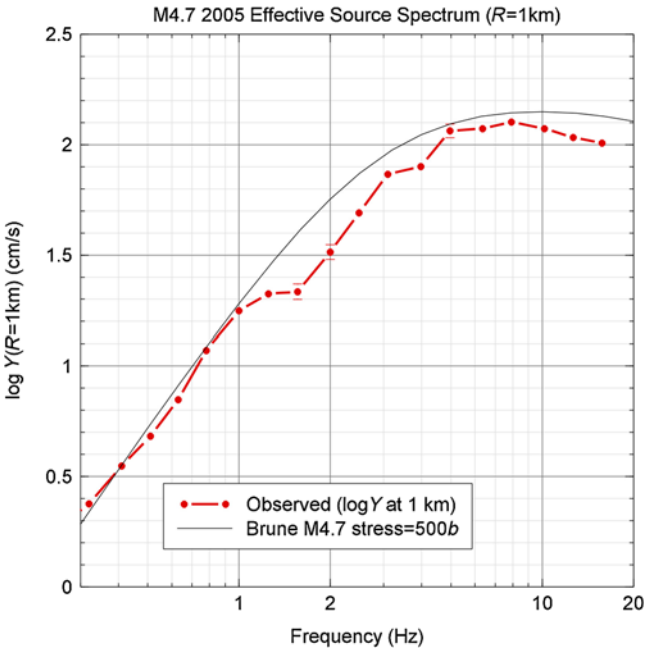

Figure 11. Effective source spectra (with standard error bars) at a distance of 1 km from the source for **M** 4.7 Rivière du Loup event, in comparison to the Brune-model spectra for 500 bar stress. The color version of this figure is available only in the electronic edition.

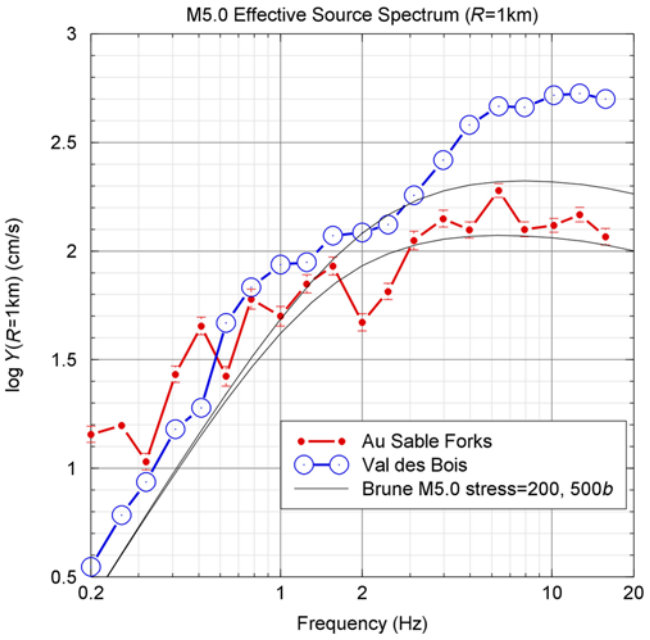

Figure 12. Effective source spectra (with standard error bars) at a distance of 1 km from the source for **M** 5.0 events, in comparison to the Brune-model spectra for 200 and 500 bar stress. The color version of this figure is available only in the electronic edition.

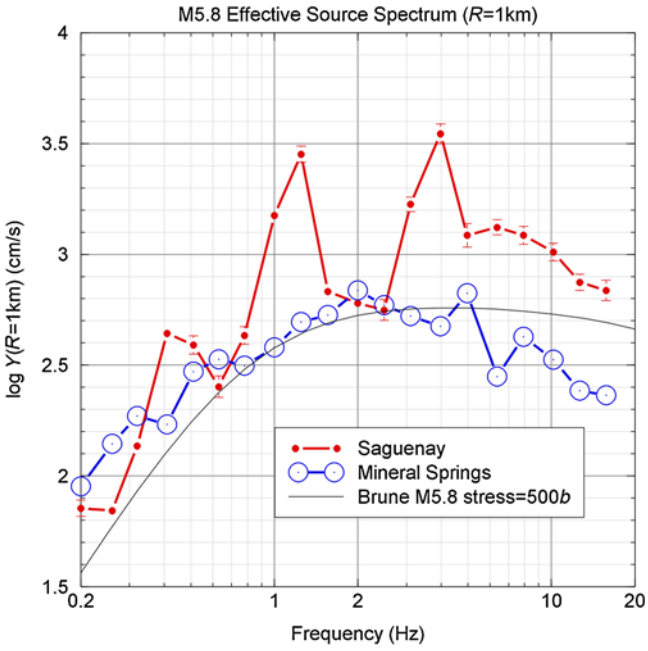

Figure 13. Effective source spectra (with standard error bars) at a distance of 1 km from the source for **M** 5.8 events, in comparison to the Brune-model spectra for 500 bar stress. The color version of this figure is available only in the electronic edition.

contaminated by noise. We estimated the observed 1 Hz source amplitude by taking a three-point average of the (log) values around 1 Hz (0.8, 1.0, 1.2 Hz values). We compared this with the predicted value of the long-period spectral level based on the Brune model for the corresponding seismic moment, assuming that for small events 1 Hz is on the displacement end of the spectrum. The difference between the observed and predicted log values (at 1 Hz) is the calculated adjustment factor required. For the larger events (**M** ≥4.5), the assumption that the 1 Hz amplitude is on the displacement end of the spectrum is not valid (amplitudes are dropping progressively lower than that expectation as the corner frequency is approached). Furthermore, we have usable signal at frequencies below 1 Hz for most of the larger events. Therefore, for events of **M** ≥4.5 the adjustment factor was determined by inspection as the shift is required to bring the Brune-model spectrum and the observations into agreement on average over the usable part of the low-frequency band (typically 0.5–1.0 Hz).

It is observed on Figure 14 that the required offset is zero on average (this was a condition that the attenuation model was required to satisfy, as described previously). We also plot the Brune stress parameter required to match the high-frequency level of the effective source spectra, both before and after shifting the spectra by the adjustment needed to match the moment constraint. The average log stress for events of **M** ≥4.5 is somewhat lower after the adjustments (2.74 versus 2.99); and, more importantly, the standard deviation of log stress is lower after the adjustment is made (0.32 versus 0.48). Overall, the average stress drop to associate with this attenuation model is ~600 bars, which applies for events of **M** ≥4.5. As noted by Boore *et al.* (2010), this stress is tied to the steep attenuation rates that are assumed to apply from the source to 50 km. A slower attenuation would

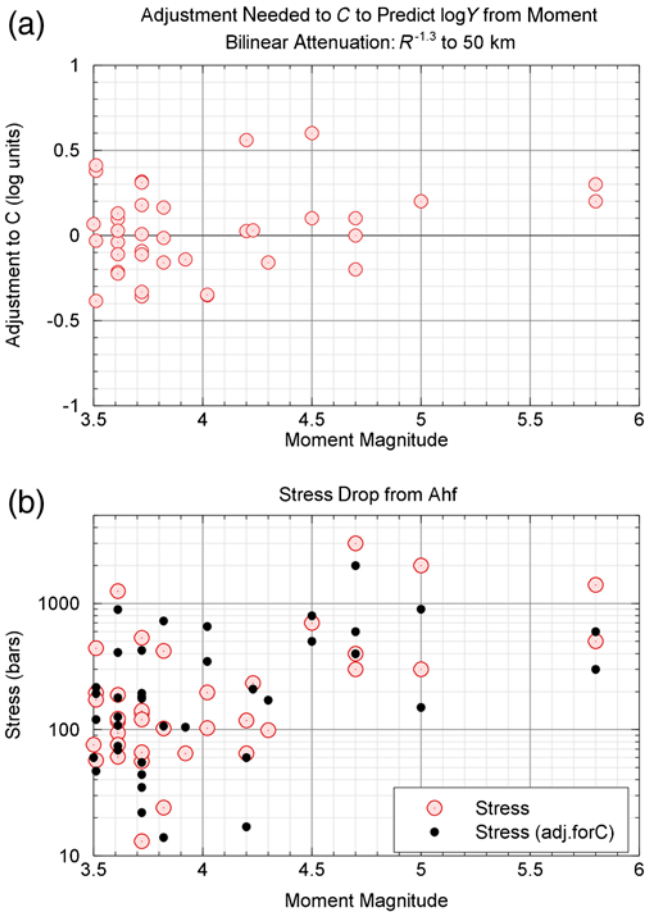

Figure 14. (a) Adjustment to constant C needed to match low-frequency effective source spectral amplitudes to moment constraint. (b) Brune stress parameter, before and after adjusting constant C. The color version of this figure is available only in the electronic edition.

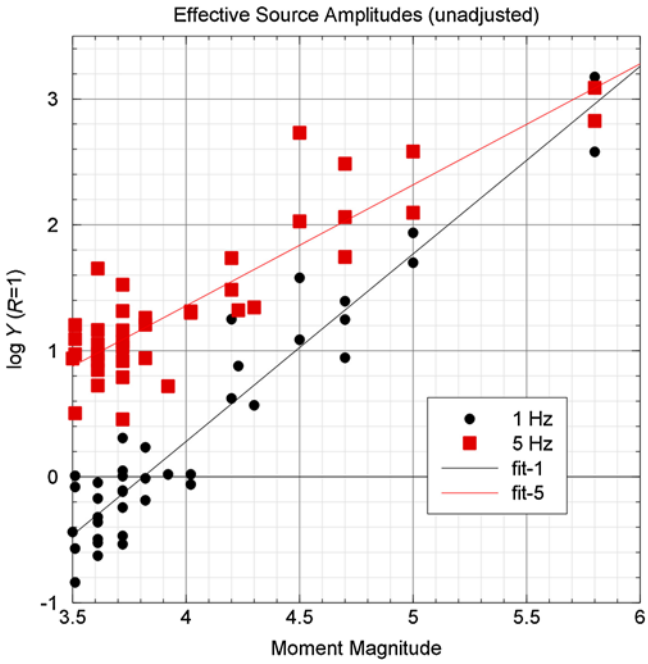

Figure 15. Effective source amplitudes ($R = 1$ km) versus moment magnitude, at 1 and 5 Hz. The color version of this figure is available only in the electronic edition.

imply lower stresses, in order to match the same observations at regional distances (see also E. Yenier and G. M. Atkinson, unpublished manuscript, 2014). Thus, it is important to recognize that these stress parameters can only be used in the context of the whole package, including the specified steep attenuation from the source. This is why the stress parameters for these events are much higher than typical values inferred from other studies that used a lower attenuation rate (as shown by Boore *et al.*, 2010). Furthermore, it means that the stress parameters from this study cannot be readily compared with values obtained for events in other regions, from other studies that used different attenuation rates. A more meaningful point of comparison in this respect would be the actual predicted ground-motion spectra at physically realizable distances (e.g., epicentral distances > 0).

Another interesting feature that is observed in Figure 14 is that the stress parameter values are magnitude dependent, with events of **M** < 4.5 having noticeably lower stress parameter values. This is in accord with previous studies (Atkinson, 1993; Mereu *et al.*, 2013) that have reported magnitude-dependent stress implying non-self-similar scaling for small events in ENA. This is not a bandwidth effect (i.e., a possible consequence of having insufficient bandwidth at high frequencies to see the high-frequency level) because we can readily verify by inspection of the source spectra of the study events that the high-frequency level, and thus the stress parameter is well defined for most events of **M** > 3.6. Mereu *et al.* (2013) point out that the observed scaling behavior of the stress parameter at lower magnitudes is consistent with the theoretical expectations based on constant-width scaling of fault size with magnitude. Further study of the source characteristics of ENA events is clearly important but remains a challenging task due to the lack of near-source observations over a suitable magnitude range.

Finally, we can look at the effective source amplitudes as a function of magnitude to develop an average model of effective source spectra. Figure 15 plots the inferred 1 and 5 Hz amplitudes at $R = 1$ km (after correcting for the attenuation model) versus magnitude, along with linear best-fit lines. The adjustment factors for the source terms, as indicated in Figure 14, are not applied in these plots, as the point is to show the inferred trend of the source amplitudes with magnitude that are present in the actual data (before the interpreted adjustment factors to match the moments). The coefficients of the lines are given in Table 1. We caution that these fit lines are not well constrained by data above **M** 5 and should not be extrapolated beyond the data range. We use the coefficients of the fitted lines to predict the average effective source spectrum for **M** 3.5, 4.5, and 5.5 that are suggested by the data, and we show these on Figure 16 in comparison to a standard Brune model for a stress of 500 bars. Overall, the

Table 1
Coefficients of $\log A(R=1) = c_0 + c_1\mathbf{M}$

Frequency	c_0	c_1
0.20	−5.10	1.20
0.26	−4.95	1.18
0.32	−5.61	1.34
0.41	−6.29	1.52
0.51	−6.35	1.55
0.63	−6.09	1.50
0.78	−5.78	1.47
1.00	−5.67	1.49
1.25	−5.26	1.43
1.56	−4.50	1.28
2.00	−4.04	1.20
2.49	−3.54	1.12
3.10	−3.24	1.09
3.98	−2.99	1.06
4.96	−2.48	0.96
6.36	−2.00	0.87
7.92	−1.80	0.83
10.17	−1.42	0.75
12.65	−1.07	0.67
15.74	−0.91	0.63

effective source spectra appear to be in good agreement with the 500 bar Brune point-source model. The deviations at $f < 1$ Hz for $\mathbf{M} < 5$ are largely attributable to the commonly observed noise peak near 0.3 Hz (e.g., Peterson, 1993), which swamps the actual signal for small events. The effective source spectra are slightly above this level at **M** 5.5, because the adjustment constant is positive for the four largest events in our dataset (as seen in Figs. 12 and 13). For all four of these events, the ground motions observed at both low and high frequencies were somewhat larger than would be suggested by their moment magnitudes. It is not known whether this is a general feature of such events in ENA or merely a random result from a very small sample of such events.

Conclusions

Fourier spectral amplitudes for events of **M** 3.5–5.8 in ENA (specifically the region of ENA that includes southeastern Canada and the northeastern United States) can be modeled with a Brune point-source model with a stress parameter of approximately 500–600 bars. The high near-source ground-motion amplitudes that are implied by such a large stress value decay steeply within 50 km of the source, with an effective geometric spreading rate of $1/R^{1.3}$. Beyond 50 km, amplitudes are well modeled with a geometric spreading rate of $1/R^{0.5}$ and an associated $Q = 525f^{0.45}$. This attenuation model is similar to that reported by Boatwright and Seekins (2011), with the important exception of our finding of a steeper near-distance geometric spreading rate. The steeper effective geometric spreading at $R < 50$ km is strongly supported by the amplitude data. The data also suggest that the effective geometric spreading has some frequency-dependent features. We have chosen to model such

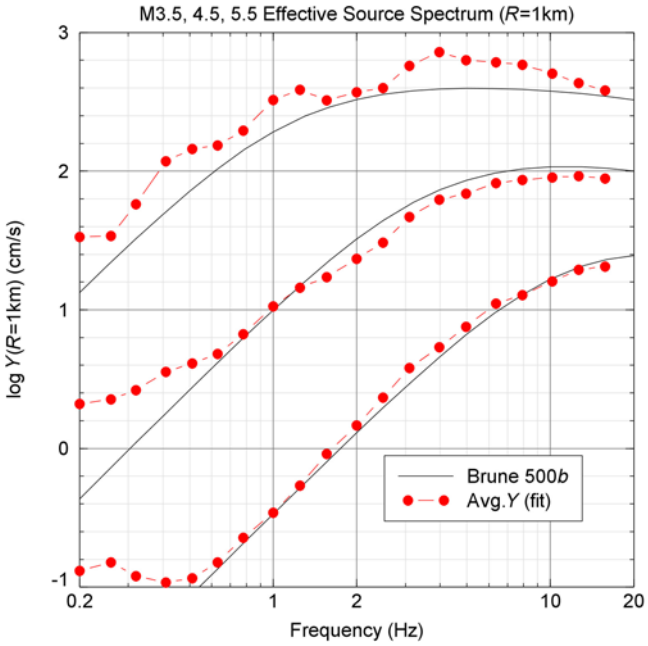

Figure 16. Fitted model amplitudes at source for **M** 3.5, 4.5, and 5.5 in comparison to the Brune model with stress = 500 bars. The noise contamination of the spectrum at $f < 1$ Hz for $\mathbf{M} < 5$ is noted. The color version of this figure is available only in the electronic edition.

features as empirical amplitude adjustment factors that could potentially be attributed to a number of factors, including the possibility that complex source and radiation effects do not average out over the focal sphere. Understanding such effects is the subject of future investigations. The applicability of the attenuation model to other parts of ENA, including the central United States (New Madrid) is also the subject of future investigations.

Data and Resources

The database for study is the Fourier amplitude database for event in ENA as compiled and processed by Assatourians and Atkinson (2010; www.seismotoolbox.ca, last accessed May 2013), updated through 2011. Moment magnitudes were extracted from R. B. Herrmann's Moment Tensor Solution website (http://www.eas.slu.edu/eqc/eqc_mt/MECH.NA/; last accessed August 2012). Moment tensors for moderate-to-large events ($\mathbf{M} > 5$) can be obtained by the Global Centroid Moment Tensor project (www.globalcmt.org; last accessed September 2012). Figures in this study were produced by CoPlot software. **M** values were estimated for the remainder of the events using regional amplitude data calibrated to events with known moment as described by Atkinson and Babaie Mahani (2013).

Acknowledgments

Funding for this study was provided by the U.S. Nuclear Regulatory Commission as part of the Next Generation Attenuation-East Project. We

thank Christine Goulet, Rasool Anooshehpoor, Shahram Pezeshk, John Douglas, Brad Aagard, and an anonymous reviewer for their constructive comments.

References

Anderson, J., and S. Hough (1984). A model for the shape of the Fourier amplitude spectrum of acceleration at high frequencies, *Bull. Seismol. Soc. Am.* **74,** 1969–1993.

Assatourians, K., and G. M. Atkinson (2010). Database of processed time series and response spectra data for Canada: An example application to study of 2005 MN 5.4 Riviere du Loup, Quebec, earthquake, *Seismol. Res. Lett.* **81,** 1013–1031.

Atkinson, G. M. (1993). Source spectra for earthquakes in eastern North America, *Bull. Seismol. Soc. Am.* **83,** 1778–1798.

Atkinson, G. M. (2004). Empirical attenuation of ground-motion spectral amplitudes in southeastern Canada and the northeastern United States, *Bull. Seismol. Soc. Am.* **94,** 1079–1095.

Atkinson, G. M. (2012). Evaluation of attenuation models for the northeastern United States/southeastern Canada, *Seismol. Res. Lett.* **83,** 166–178.

Atkinson, G. M., and A. Babaie Mahani (2013). Estimation of moment magnitude from ground motions at regional distances, *Bull. Seismol. Soc. Am.* **103,** 107–116.

Atkinson, G. M., and D. M. Boore (1995). New ground motion relations for eastern North America, *Bull. Seismol. Soc. Am.* **85,** 17–30.

Atkinson, G. M., and D. M. Boore (2006). Earthquake ground-motion prediction equations for eastern North America, *Bull. Seismol. Soc. Am.* **96,** 2181–2205.

Atkinson, G. M., and R. Mereu (1992). The shape of ground motion attenuation curves in southeastern Canada, *Bull. Seismol. Soc. Am.* **82,** 2014–2031.

Atkinson, G. M., and W. Silva (2000). Stochastic modeling of California ground motions, *Bull. Seismol. Soc. Am.* **90,** 255–274.

Babaie Mahani, A., and G. M. Atkinson (2012). Evaluation of functional forms for attenuation of small-to-moderate-earthquake response spectral amplitudes in North America, *Bull. Seismol. Soc. Am.* **102,** 2714–2726.

Benz, H., A. Frankel, and D. Boore (1997). Regional *Lg* attenuation for the continental United States using broadband data, *Bull. Seismol. Soc. Am.* **87,** 606–619.

Boatwright, J., and L. Seekins (2011). Regional spectral analysis of three moderate earthquakes in northeastern North America, *Bull. Seismol. Soc. Am.* **101,** 1769–1782.

Boore, D. M. (1983). Stochastic simulation of high-frequency ground motions based on seismological models of the radiated spectra, *Bull. Seismol. Soc. Am.* **73,** 1865–1894.

Boore, D. M. (2003). Simulation of ground motion using the stochastic method, *Pure Appl. Geophys.* **160,** 635–676.

Boore, D. M. (2009). Comparing stochastic point-source and finite-source ground-motion simulations: SMSIM and EXSIM, *Bull. Seismol. Soc. Am.* **99,** 3202–3216.

Boore, D. M., K. W. Campbell, and G. M. Atkinson (2010). Determination of stress parameters for eight well-recorded earthquakes in eastern North America, *Bull. Seismol. Soc. Am.* **100,** 1632–1645.

Brune, J. N. (1970). Tectonic stress and the spectra of seismic shear waves from earthquakes, *J. Geophys. Res.* **75,** 4997–5009.

Brune, J. N. (1971). Correction, *J. Geophys. Res.* **76,** 5002.

Burger, R., P. Somerville, J. Barker, R. Herrmann, and D. Helmberger (1987). The effect of crustal structure on strong ground motion attenuation relations in eastern North America, *Bull. Seismol. Soc. Am.* **77,** 420–439.

Chapman, M. (2012). Modeling near-source geometrical spreading and the relative amplitudes of vertical and horizontal high-frequency ground motions in eastern North America, *Bull. Seismol. Soc. Am.* **102,** 1957–1975.

Lermo, J., and F. J. Chavez-Garcia (1993). Site effect evaluation using spectral ratios with only one station, *Bull. Seismol. Soc. Am.* **83,** 1574–1594.

Mereu, R., S. Dineva, and G. M. Atkinson (2013). The application of velocity spectral stacking to extract information on source and path effects for small-to-moderate earthquakes in southern Ontario with evidence for constant width faulting, *Seismol. Res. Lett.* **84,** 899–916.

Ou, G., and R. Herrmann (1990). A statistical model for peak ground motion from local to regional distances, *Bull. Seismol. Soc. Am.* **80,** 1397–1417.

Peterson, J. (1993). Observations and modelling of background seismic noise, *U.S. Geol. Surv. Open-File Rept. 93-322*, Albuquerque, New Mexico.

Shin, T., and R. Herrmann (1987). *Lg* attenuation and source studies using 1982 Miramichi data, *Bull. Seismol. Soc. Am.* **77,** 384–397.

Siddiqqi, J., and G. M. Atkinson (2002). Ground motion amplification at rock sites across Canada, as determined from the horizontal-to-vertical component ratio, *Bull. Seismol. Soc. Am.* **62,** 877–884.

Yenier, E., and G. M. Atkinson (2012). Stochastic modeling of the source and attenuation characteristics of moderate-to-large magnitude earthquakes: Investigation of apparent distance saturation effects (abstract), *Seismol. Res. Lett.* **83** (Annual Meet.).

Western University
Department of Earth Sciences
London, Ontario N6A 5B7
gmatkinson@aol.com
(G.M.A.)

U.S. Geological Survey
345 Middlefield Rd.
Menlo Park, California 94205
boore@usgs.gov
(D.M.B.)

Manuscript received 24 May 2013;
Published Online 26 November 2013